Micro X-ray CT imaging of pore-scale changes in unconsolidated sediment under confining pressure

Mandy Schindler[(1)] *and Manika Prasad*[*]*, Center for Rock Abuse, Colorado School of Mines, USA*

(1) correspondence email: manschin@mines.edu

SUMMARY

Micro X-ray computed tomography was used to image confining-pressure induced changes in a dry, unconsolidated quartz sand pack while simultaneously recording ultrasonic P-wave velocities. The experiments were performed under in-situ pressure of up to 4000 psi. We visually observed a reduction in porosity by more than a third of the initial value as well as extensive grain damage, changes in pore and grain size distribution and an increase in contact number and contact radius with increasing confining pressure. We further used porosity, contact number and contact radius to model P-wave velocity with the contact-radius model by Bachrach et al. (1998).

INTRODUCTION

Micro X-ray computed tomography (μCT) is an efficient, non-destructive 3D imaging technique. It is applied to porous materials to characterize pore and grain size distribution, pore morphology, pore fluids and hydraulic properties (Dvorkin et al., 2011; Madonna et al., 2013; Saenger et al., 2016). The majority of digital rock physics studies rely on μCT images obtained under ambient pressure and temperature conditions (Andrä et al., 2013), although effective rock properties strongly depend on in situ conditions. Thus, we implemented a pressure control system for use inside the Xradia-400 μCT machine (Figure 1). Goal of this work is to be able to obtain μCT images of rock samples while pore and confining pressure is applied. In addition to pressure control we recorded ultrasonic P-wave velocities simultaneously with μCT imaging. The combination of imaging and velocity measurements provides insight in pore-scale changes in the rock and their influence on elastic properties.

EXPERIMENTAL METHOD

The Xradia-400 micro X-ray CT works at a maximum source power of 10 W and source voltage of 150 keV. The maximum size of field of view is 2 by 2 inches (50.8 mm * 50.8 mm). The highest resolution is 1 μm. For high resolution scans the field of view is significantly smaller (e.g. for a resolution of 1 μm the field of view is reduced to 1 mm by 1 mm) and for a big field of view the resolution is reduced (e.g. for maximum size of field of view, resolution is 70 μm). The required representative sample size counteracts the maximum achievable resolution of μCT images. Thus, we used a medium resolution (5 μm) and medium size of field of view (5 mm * 5 mm).

Figure 1 shows a schematic of the experimental setup inside the μCT machine. Confining pressure is applied through an

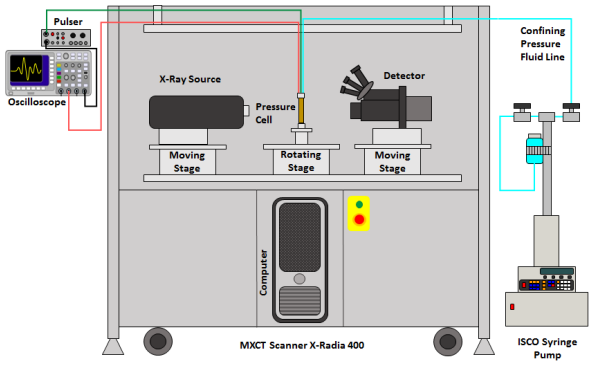

Figure 1: Schematic of the μCT machine with pressure vessel, pressure control systems and ultrasonic setup

ISCO pump located outside of μCT machines lead enclosure. We use hydraulic oil as a confining fluid. A pulser and an oscilloscope are connected to the two ultrasonic transducers inside the pressure vessel. Feed-throughs on top of the vessel allow to attach 4 wires and 2 fluid lines (confining and pore pressure). Pore pressure was not applied during this study.

The pressure vessel consists of an aluminum rod with stainless steel Swagelog fittings on both ends. The vessel has an outer diameter of 25.4 mm (1 inch) and an inner diameter of 20.6 mm. It has been tested for pressures up to 5000 psi (34.5 MPa). We chose aluminum as material for the pressure vessel since it proved to withstand high pressures while having a low density and thus being transparent to X-rays. Higher density materials, like stainless steel, would cause significant attenuation of X-rays and thus a much longer scanning time and artefacts in the CT images.

We built ultrasonic transducers that can be used within the spatial constraints of the pressure vessel (Figure 2). The transducers consist of piezoelectric PZT P-wave crystals with a diameter of 4 mm encased by cylindrical pieces of PEEK (12.6 mm diameter). The small dimensions of the transducers led us to the decision to include only P-wave crystals for now. Pore fluid lines are added to both transducers. The top transducer has a stainless steel fluid line which is connected to the feed-through pore fluid line with a Swagelok fitting and holds the sample in place during the imaging process.

The sample shown in Figure 3 consists of a 21 mm long sediment pack placed between the two ultrasonic transducers. The sample was jacketed with heat shrink tubing and clamped with steel wires on both ends. As sediment we used coarse grained quartz sand with an average grain size of 1 mm. The sample was dry; pore pressure was not applied.

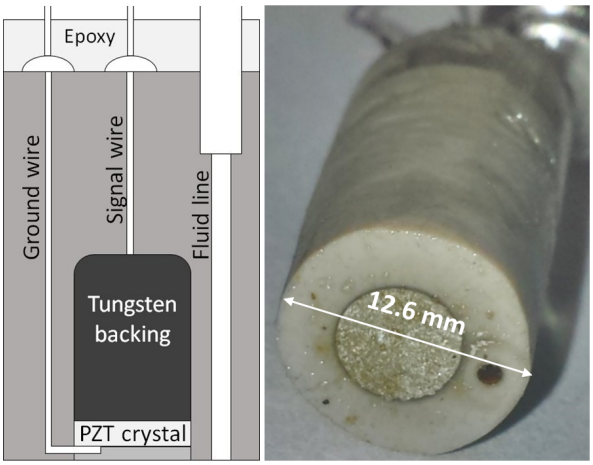

Figure 2: Ultrasonic P-wave transducers for use in μCT pressure vessel

Figure 3: Sample of coarse-grained quartz sand between 2 ultrasonic transducers, covered with a heat-shrink sleeve, length: 21 mm, diameter: 12.6 mm

Table 1: Porosity, average grain size and average pore size for different pressures from micro CT images

P_C [psi]	ϕ[v/v]	grain size [μm]	pore size [μm]
12 (before)	0.377	1180	N/A
500	0.362	1170	1110
1000	0.344	1180	1030
2000	0.309	1150	1030
3000	0.273	1140	820
4000	0.245	1160	760
12 (after)	0.248	1080	740

We recorded μCT images and ultrasonic velocities at 10 pressure steps: starting from 12 psi (atmospheric pressure) we increased the pressure in 500 psi steps until 4000 psi and then decreased the pressure back to atmospheric pressure. A pressure gradient of 50 psi/min was applied between each measurement stage. The μCT imaging took approximately 14 hours for each pressure step.

Image analysis was performed in Matlab and imageJ. We used a median filter combined with a derivative filter and gray value thresholding to obtain porosities, pore size and grain size distributions from the μCT images.

RESULTS

Figure 4 shows horizontal slices through the sample at 5 different confining pressures and after decreasing the pressure to atmospheric pressure after the experiment. We observed grain damage throughout the entire sample, especially near contact points between two adjacent grains with a small contact radius. Grains that were separated by pore space at atmospheric pressure are crushed against each other at elevated pressure which leads to fracturing. A strong porosity decrease from 0.377 at atmospheric pressure to 0.245 at 4000 psi confining pressure was observed (Table 1). Both, fracturing and compaction are a continuous process observed during all pressure steps. At higher pressure previous fractures extended further and additional fractures formed. Average grain size and pore size distribution require further refinement since the current algorithm is not able to separate adjacent grains and pores leading to an overestimation of grain and pore size. We observed a slight decrease in average grain size which can be attributed to the fracturing of larger grains into smaller grain fragments and a decrease in pore size due to the compression of the sample leading to porosity reduction. The particle analysis will be performed in 3D as we continue the work on this dataset.

Figure 5 shows ultrasonic P-wave signals recorded at all confining pressure steps and their first arrival. We observed a strong increase in P-wave velocity from 543 m/s to 1466 m/s. This strong increase can be attributed to a decrease in velocity and an increase in contact number and contact radius (Digby, 1981).

μCT imaging under confining pressure

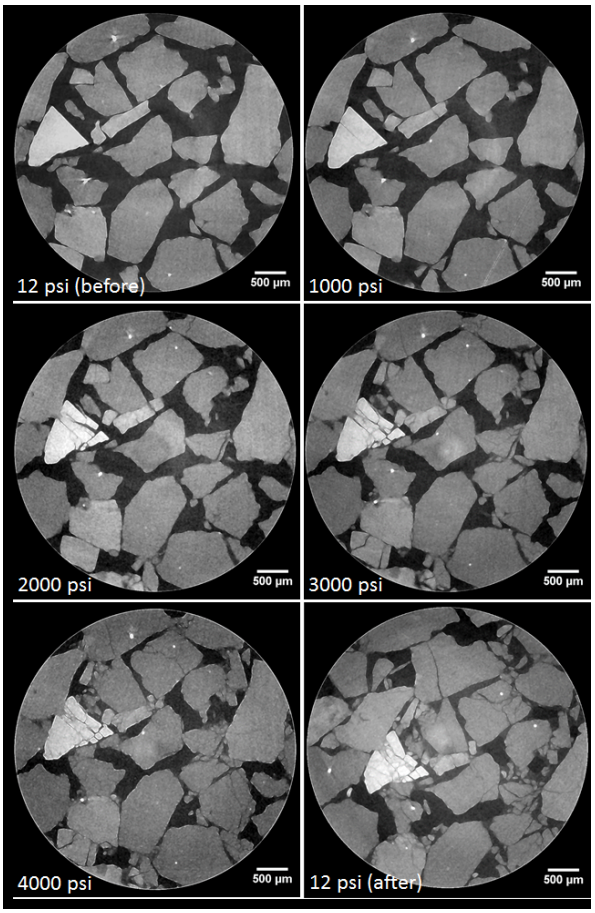

Figure 4: Horizontal slices of μCT images at five different confining pressures from atmospheric pressure to 4000 psi. Porosity reduction, an increase in grain contact points and radius and grain crushing with associated fracturing was observed. The image at atmospheric pressure after the experiment was performed shows that grain damage and porosity reduction are irreversible

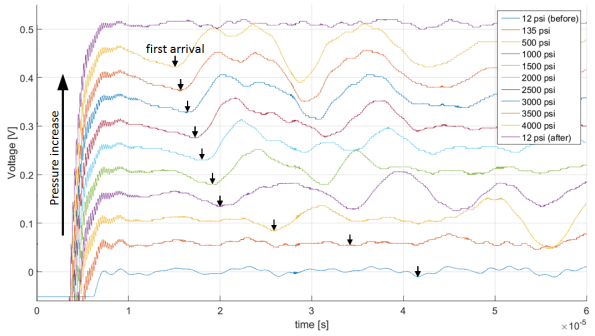

Figure 5: Compressional ultrasonic waveforms for all confining pressure steps. First arrival times decrease with increasing confining pressure

Table 2: Ultrasonic velocities

P_C [psi]	v_p [m/s]
12	543
135	650
500	875
1000	1141
1500	1176
2000	1237
2500	1288
3000	1359
3500	1410
4000	1466

Table 3: contact number (n), contact radius (a) and modeled P-wave velocity

P_C [psi]	ϕ[v/v]	n	a [μm]	v_p [m/s]
500	0.362	3.6	102	1277
3000	0.273	5.5	155	1969

Figure 6 and Table 3 show the change in contact radius between 500 psi and 3000 psi confining pressure. We measured all contact points for 20 grains in the sample and observed an increase of the average contact number from 3.6 to 5.5 and an increase in average contact radius from 102 μm to 155 μm.

These values can be used as input parameters for models of elastic properties. We chose to use the contact-radius model by Bachrach et al. (1998). The equations

$$S_n = \frac{4aG}{1-\nu} \qquad S_t = \frac{8aG}{2-\nu}$$

$$K_= \frac{n(1-\Phi)}{12\pi R_g} S_n \qquad G_= \frac{n(1-\Phi)}{20\pi R_g}(S_n + 1.5S_t)$$

$$v_p = \sqrt{\frac{K+4/3G}{\rho}}$$

describe how P-wave velocity is related to ϕ - porosity, n - average contact number, a - average contact radius and R_g - average grain radius (values from μCT imaging in Tables 1 and 3. Other parameters are G - shear modulus (38 GPa for quartz), ν - Poisson's ratio (0.15 in Bachrach et al. (1998)), ρ - bulk density, obtained from grain density of quartz and porosity.

The grain contact number n is commonly assumed to be 9, the contact number of an ideal pack of identical spheres. Digby (1981) use a number of 8.84. Despite our smaller grain contact number, the modeled velocities are far higher than the measured ultrasonic velocities. For 3000 psi our low ultrasonic velocity could be a result to the extensive grain damage which is not taken into account by the contact radius model. A more thorough analysis of contact radius and average grain size in 3D might result in a better match of measured and modeled compressional velocities.

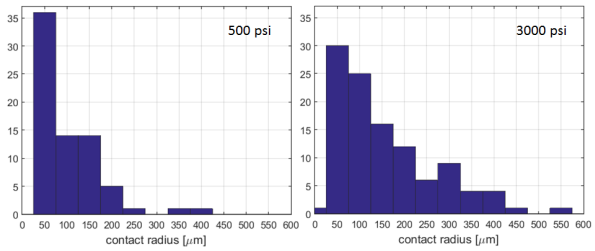

Figure 6: Histograms of contact radii of 20 grains at 500 psi and 3000 psi. An increase in contact radius was observed with increasing pressure

CONCLUSIONS AND FUTURE WORK

We were able to prove the functionality of our pressure control system and demonstrated that changes in rock samples can be visually observed within the resolution constraints of the Xradia-400 machine. We developed a pressure vessel and ultrasonic transducers suitable for the use in the μCT machine.

We observed compaction of the sample upon confining pressure increase resulting in extensive grain damage and fracturing of sediment grains during each pressure step. Porosity was decreased by more than a third of its initial value. Grain damage and porosity reduction are irreversible; the initial state of the sample is not recovered when decreasing confining pressure back to atmospheric pressure. An increase in ultrasonic P-wave velocities with increasing pressure was observed. We will continue our efforts to model our velocity response based on the parameters obtained from μCT images (porosity, contact number, contact radius). The Bachrach contact-radius model confirmed an increase in P-wave velocities but did not match our measured data.

We will conduct further studies on consolidated rock samples and will repeat experiments on unconsolidated sand packs with a smaller pressure gradient. A more thorough analysis of grain and pore size distribution will be performed in 3D in order to obtain pore and bulk compressibilities.

ACKNOWLEDGEMENTS

We thank Jyoti Behura for his advice on image processing, Manju Murugesu who helped with image analysis, and Azar Hasanov whose sample inspired this study.

This material is based upon work supported by the U.S. Department of Energy (DOE) under Grant Number DEFE0009963. This project is managed and administered by the Colorado School of Mines and funded by DOE/NETL and cost-sharing partners. This report was prepared as an account of work sponsored by an agency of the United States Government. Neither the United States Government nor any agency thereof, nor any of their employees, makes any warranty, express or implied, or assumes any legal liability or responsibility for the accuracy, completeness, or usefulness of any information, apparatus, product, or process disclosed, or represents that its use would not infringe privately owned rights. Reference herein to any specific commercial product, process, or service by trade name, trademark, manufacturer, or otherwise does not necessarily constitute or imply its endorsement, recommendation, or favoring by the United States Government or any agency thereof. The views and opinions of authors expressed herein do not necessarily state or reflect those of the United States Government or any agency thereof.

REFERENCES

Andrä, H., N. Combaret, J. Dvorkin, E. Glatt, J. Han, M. Kabel, Y. Keehm, F. Krzikalla, M. Lee, C. Madonna, et al., 2013, Digital rock physics benchmarkspart i: Imaging and segmentation: Computers & Geosciences, **50**, 25–32.

Bachrach, R., J. Dvorkin, and A. Nur, 1998, High-resolution shallow-seismic experiments in sand, part ii: Velocities in shallow unconsolidated sand: Geophysics, **63**, 1234–1240.

Digby, P., 1981, The effective elastic moduli of porous granular rocks: Journal of Applied Mechanics, **48**, 803–808.

Dvorkin, J., N. Derzhi, E. Diaz, and Q. Fang, 2011, Relevance of computational rock physics: Geophysics, **76**, E141–E153.

Madonna, C., B. Quintal, M. Frehner, B. S. Almqvist, N. Tisato, M. Pistone, F. Marone, and E. H. Saenger, 2013, Synchrotron-based x-ray tomographic microscopy for rock physics investigations: Geophysics, **78**, D53–D64.

Saenger, E. H., M. Lebedev, D. Uribe, M. Osorno, S. Vialle, M. Duda, S. Iglauer, and H. Steeb, 2016, Analysis of high-resolution x-ray computed tomography images of bentheim sandstone under elevated confining pressures: Geophysical Prospecting, **64**, 848–859.